J Mater Sci: Mater Electron (2015) 26:4880–4887
DOI 10.1007/s10854-015-2997-0

Hydrothermal synthesis and microwave absorption properties of Fe_3O_4@SnO_2 core–shell structured microspheres

Yanping Wang[1] · Zheng Peng[1] · Wei Jiang[1]

Received: 21 December 2014 / Accepted: 23 March 2015 / Published online: 27 March 2015

Abstract Fe_3O_4@SnO_2 core–shell structured microspheres have been designed and synthesized by a simple hydrothermal method. The transmission electron microscopy and scanning electron microscopy characterization results indicate that SnO_2 nanoparticles were successfully grown on the surface of Fe_3O_4 microspheres with different sizes. The X-ray diffractograms show that the nanocomposites are composed of cubic Fe_3O_4 and tetragonal SnO_2. The magnetic hysteresis measurements reveal the ferromagnetic behavior of the nanocomposites at room temperature. Considering that both Fe_3O_4 and SnO_2 are good microwave absorption materials, we have investigated the microwave absorption properties by a vector network analyzer between 2 and 18 GHz at room temperature. The electromagnetic data demonstrate that the as-synthesized Fe_3O_4@SnO_2 microspheres exhibit extraordinary microwave absorption properties, which may result from the proper electromagnetic match and interface polarization between the Fe_3O_4 cores and SnO_2 shells. Moreover, a possible formation mechanism of Fe_3O_4@SnO_2 microspheres based on the hydrothermal method was also proposed.

1 Introduction

With the serious electromagnetic interference pollution arising from radar systems, local area network systems and various electronic devices, microwave absorption materials with strong absorption characteristics, wide absorption frequency and high thermal stability have attracted much attention [1, 2]. Magnetite (Fe_3O_4) nanoparticles have been widely studied as the traditional absorber due to their low cost and excellent microwave absorption properties [3, 4]. However, Fe_3O_4 nanoparticles are unable to maintain stability and are easily oxidized, which hamper their applications. Therefore, it should be promising and meaningful to synthesis Fe_3O_4-based nanocomposites.

Tin oxides (SnO_2), as a multifunctional n-type semiconductor, has been widely used as gas sensor, anode material and photocatalyst due to its unique gas sensitivity, high conductivity and catalytic properties [5, 6]. Further, SnO_2 has temperature and environmentally stable dielectric properties, which have an advantage in the area of microwave absorbers. Generally, the excellent microwave absorptions are strongly dependent on the efficient complementarities between the relative permittivity and permeability [7]. The combination of magnetic materials and dielectric materials may combine their special magnetic and dielectric properties, providing opportunities for achieving excellent microwave absorption properties. It is well known that one-dimensional core–shell nanostructures have shown exciting physical properties due to the potential to combine or cooperation the individual properties of each component [8]. Among all core–shell nanocomposites, composed of Fe_3O_4 cores and nonmagnetic shells are especially focused on. For example, Fe_3O_4@SiO_2 core–shell nanoparticles were prepared by the reverse microemulsion method [9], Fe_3O_4@ZnO core–shell nanoparticles were synthesized by a simple one-pot sequential polyol process [10]. Fe_3O_4@TiO_2 core–shell microspheres were fabricated by combining a solvothermal reaction and calcination process [11]. Recently, Chen et al. [12] have successfully prepared porous Fe_3O_4/SnO_2 core–shell nanorods with excellent microwave absorption

✉ Wei Jiang
superfine_jw@126.com

[1] National Special Superfine Powder Engineering Research Center, Nanjing University of Science and Technology, Nanjing 210094, People's Republic of China

properties. To date, several methods have been reported for the fabrication of Fe_3O_4/SnO_2 nanocomposites. For instance, SnO_2/Fe_3O_4 nanocomposites hierarchical nanosheets with paramagnetic property have been synthesized by hydrothermal method [13]. Fe_3O_4–SnO_2 composites with bactericidal activity have been prepared by sonochemical methods [14]. Li et al. [15] fabricated $Fe_3O_4@SnO_2$ core–shell nanorod film with large areal capacitance and long-term cycleability directly on a Ti substrate. However, to the best of our knowledge, reports on the synthesis of $Fe_3O_4@SnO_2$ core–shell structured microspheres which may possess excellent microwave absorption properties are still scarce.

As is well known, the microwave absorption properties of a material are closely related to the composition, mean size and structure of the absorber [16]. In the present work, we carried out the synthesis of $Fe_3O_4@SnO_2$ core–shell structured microspheres with different core sizes by hydrothermal method. Owing to the less expensive, easy control process and uniform coating efficiency, our method provides a promising route for the controlled synthesis of Fe_3O_4-based core–shell structure nanocomposites. Moreover, the magnetic and microwave absorption properties of the $Fe_3O_4@SnO_2$ microspheres were investigated.

2 Experiment section

2.1 Materials and characterization

Ferric chloride hexahydrate ($FeCl_3{\cdot}6H_2O$), sodium acetate (CH_3COONa), ethylene glycol (EG), diethylene glycol (DEG), tin(IV) chloride pentahydrate ($SnCl_4{\cdot}5H_2O$), sodium hydroxide (NaOH), anhydrous ethanol. All chemicals were of analytical grade and used without further purification. The water used was purified through a Miltipore System.

Powder X-ray diffraction (XRD) patterns of the core–shell microspheres samples were obtained on a Bruker D8 Advance System with Cu K_α radiation ($\lambda = 1.5418$ Å). Transmission electron microscopy (TEM) experiments were performed on a Tecnai 12 transmission electron microscope. Field emission scanning electron microscopy (SEM) and the corresponding X-ray energy dispersive spectroscopy (EDS) analyses were taken on a Hitachi S-4800 microscopy. Their magnetic properties were characterized by a vibrating sample magnetometer (VSM, Lakeshore-736) at room temperature. The complex permittivity ε ($\varepsilon = \varepsilon' - j\varepsilon''$) and permeability μ ($\mu = \mu' - j\mu''$) were measured at room temperature by an Agilent N5244A vector network analyzer over a range of 2–18 GHz. The samples used for EM parameter measurements were prepared by dispersing the as-synthesized $Fe_3O_4@SnO_2$ microspheres into paraffin with a weight ratio of 7:3, and then pressing the mixtures into a toroidal shape with an outer diameter of 7.00 mm and inner diameter of 3.04 mm.

2.2 Synthesis of $Fe_3O_4@SnO_2$

The composites were fabricated via the following process: (1) Fe_3O_4 microspheres with the diameter about 120 nm were synthesized through a simple hydrothermal method [17]. Briefly, 0.51 g $FeCl_3{\cdot}6H_2O$ and 3.75 g NaAc were dissolved in 37.50 mL EG and 37.50 mL DEG under vigorous stirring. The mixture was then sealed in a 100 mL Teflon-lined stainless-steel autoclave and maintained at 200 °C for 8 h. After cooling to room temperature, the black products were washed with deionized water and anhydrous ethanol several times, then dried at 40 °C for 6 h under vacuum and denoted as Fe_3O_4-1. The Fe_3O_4 microspheres with the diameter about 220 nm (denoted as Fe_3O_4-2) were synthesized through the same method but increasing $FeCl_3{\cdot}6H_2O$ to 2.03 g. (2) In the preparation of $Fe_3O_4@SnO_2$ core–shell microspheres [18], 0.1 g of the above dried Fe_3O_4, 0.7 g of $SnCl_4{\cdot}5H_2O$ and 0.6 g of NaOH were mixed thoroughly in 80 mL of deionized water by ultrasonication dispersion. Afterward, the mixture was transferred into a 100 mL Teflon-lined stainless-steel autoclave and hydrothermally treated at 200 °C for 8 h. After cooling to room temperature, the obtained precipitates were washed with deionized water several times. Corresponding to the Fe_3O_4 microspheres, the $Fe_3O_4@SnO_2$ microspheres were denoted as $Fe_3O_4@SnO_2$-1 and $Fe_3O_4@SnO_2$-2.

3 Results and discussion

3.1 Synthesis and morphology analysis

Figure 1 illustrates the synthesis procedure for the $Fe_3O_4@SnO_2$ core–shell microspheres. First, The Fe_3O_4 microspheres were synthesized by a hydrothermal reaction. Second, SnO_2 deposit on the Fe_3O_4 microspheres surface to form a core–shell structure by a hydrothermal reaction using $SnCl_4{\cdot}5H_2O$ as a precursor. The formation mechanism for SnO_2 nanoparticles in the hydrothermal treatment process can be written as follows:

$$Sn^{4+} + 4OH^- \xrightarrow{\text{hydrothermal}} SnO_2 + 2H_2O.$$

Figure 2a, b shows the TEM images of the $Fe_3O_4@SnO_2$ microspheres obtained by hydrothermal treatment of Fe_3O_4 microspheres in aqueous solution containing $SnCl_4{\cdot}5H_2O$ and NaOH. It can be clearly seen that the SnO_2 nanoparticles were successfully deposited onto the surfaces of Fe_3O_4 microspheres and the mean diameters of the final microspheres are around 130 and 240 nm,

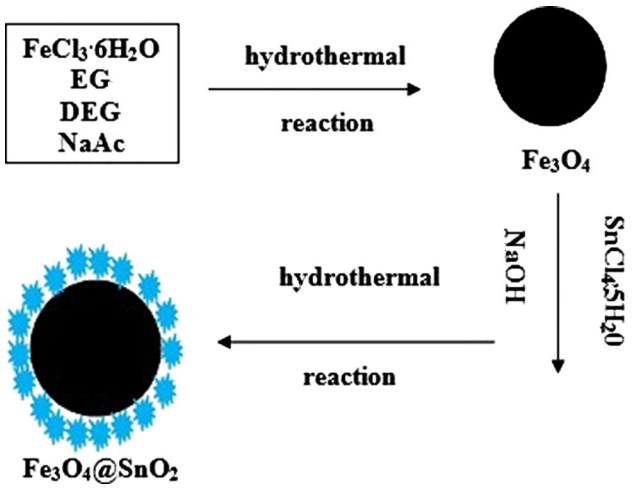

Fig. 1 Schematic diagram for the formation of the Fe_3O_4@SnO_2 core–shell microspheres

respectively. It can be also observed that the surfaces of these microspheres were not smooth, indicating the SnO_2 nanoparticles are randomly aggregated on the Fe_3O_4 microspheres' surface [19]. Furthermore, the SnO_2 shells can protect the Fe_3O_4 cores from oxidation and corrosion. Figure 3 gives the particle size distribution histograms according to the TEM images in Fig. 2a, b. As clearly seen, the particle sizes are mainly concentrated in the range of 120–140 and 230–250 nm, respectively. The particle size distribution histograms indicate that as-synthesized Fe_3O_4@SnO_2 microspheres are not only $FeCl_3 \cdot 6H_2O$ concentration-dependent size-controllable but also with the relatively narrow particle size distribution. Figure 4a, b shows the SEM images of the as-synthesized Fe_3O_4@SnO_2 microspheres. It is obvious that the microspheres exhibit a rough surface, agreeing well with the TEM observation. Moreover, both the Fe_3O_4@SnO_2-1 and Fe_3O_4@SnO_2-2 microspheres are well dispersed, suggesting that the coat-

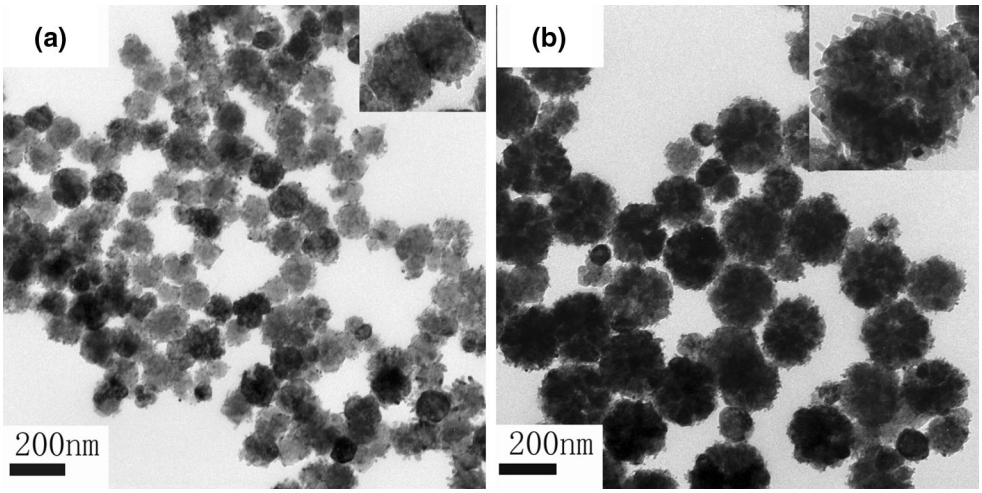

Fig. 2 TEM images of the Fe_3O_4@SnO_2 core–shell microspheres: **a** Fe_3O_4@SnO_2-1, **b** Fe_3O_4@SnO_2-2

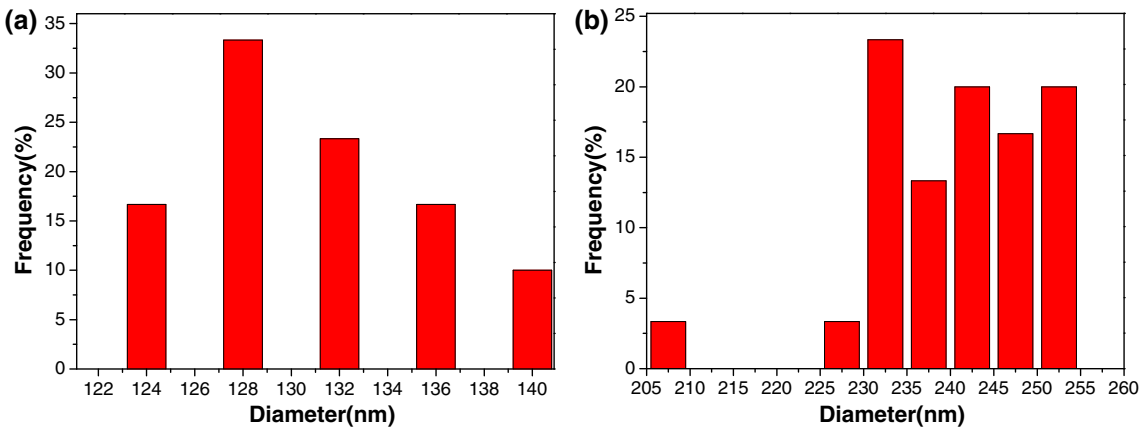

Fig. 3 The particle size distribution of the Fe_3O_4@SnO_2 core–shell microspheres: **a** Fe_3O_4@SnO_2-1, **b** Fe_3O_4@SnO_2-2

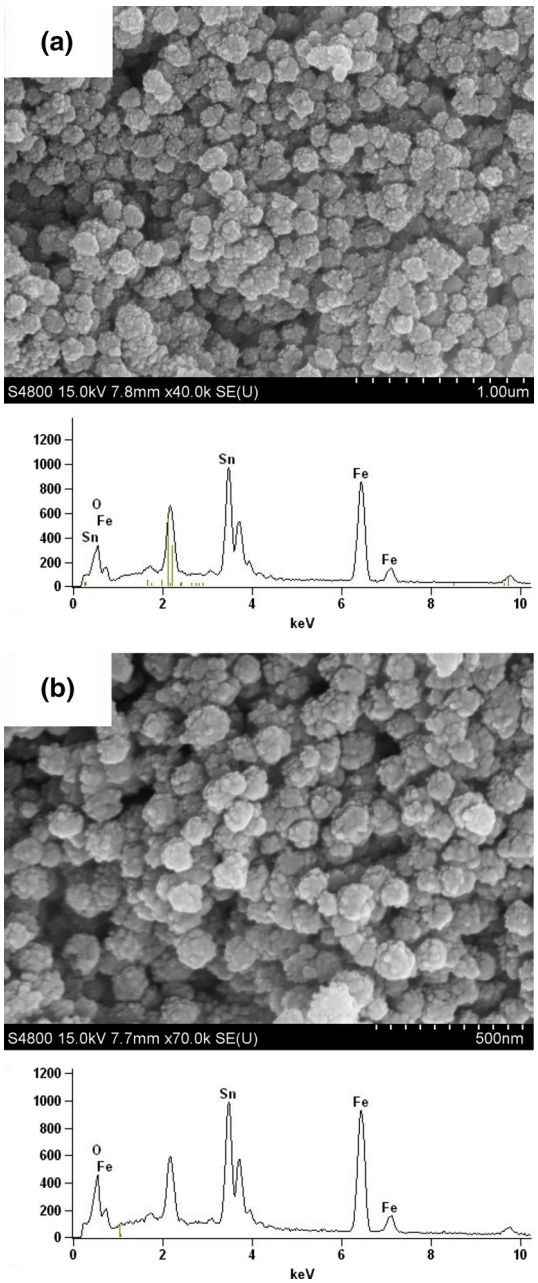

Fig. 4 SEM images and the corresponding EDS spectrum of the Fe_3O_4@SnO_2 core–shell microspheres: **a** Fe_3O_4@SnO_2-1, **b** Fe_3O_4@SnO_2-2

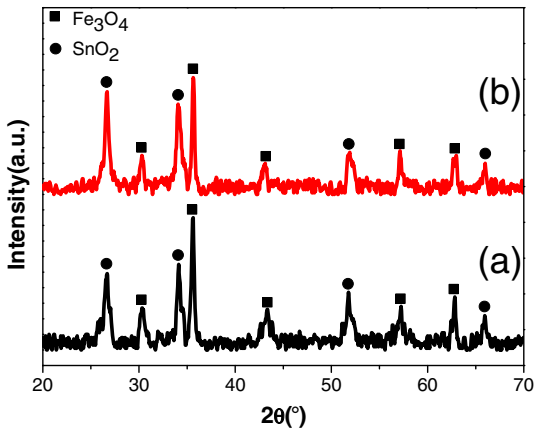

Fig. 5 XRD patterns of the Fe_3O_4@SnO_2 core–shell microspheres: (*a*) Fe_3O_4@SnO_2-1, (*b*) Fe_3O_4@SnO_2-2

ing of SnO_2 by a hydrothermal method has little effect on the dispersibility [20]. The corresponding EDS spectrum of the selected matrix area confirmed that the microspheres consisted of Fe, Sn, and O elements.

3.2 Structural properties

The XRD patterns in Fig. 5 confirm the composition of the microspheres. The diffraction peaks at $2\theta = 30.2°$, 35.6°, 43.2°, 57.0° and 62.6° can be well indexed to (220), (311), (400), (511) and (440) of cubic inverse spinel structure Fe_3O_4 (JCPDS. Card 19-0629). The extra diffraction peaks at $2\theta = 26.6°$, 33.9°, 51.6° and 65.9° correspond to the Milleer indices (110), (101), (211) and (301) planes, which can be assigned to tetragonal rutile SnO_2 (JCPDS card 41-1445). The XRD results confirm that the final composites are composed of cubic Fe_3O_4 and tetragonal SnO_2. Combined with the previous TEM, SEM and EDS results, it can be concluded that Fe_3O_4@SnO_2 core–shell structured microspheres with different Fe_3O_4 core sizes have been successfully synthesized.

3.3 Magnetic properties

The magnetic hysteresis loops of the as-synthesized microspheres are shown in Fig. 6, measured at room temperature in the applied magnetic field sweeping from −20.0 and 20.0 kOe. The main magnetic parameters including saturation magnetization (*Ms*), coercive field (*Hc*) and remnant magnetization (*Mr*) are listed in Table 1. It can be seen that the Fe_3O_4@SnO_2-1 and Fe_3O_4@SnO_2-2 shown ferromagnetic behavior with the M_S values are 34.865 and 46.284 emu/g, respectively. The relatively low *Ms* is most likely attributed to the existence of nonmagnetic SnO_2 [21, 22], but it is still large enough for effectively magnetic separation. In addition, the *Hc* values of the samples are relatively high suggesting that the high resonance frequency, which may attribute to the high surface anisotropy [12]. Moreover, significant hysteresis loops in the *M–H* curve, implying a bigger magnetic loss, which is beneficial for improving microwave absorption.

3.4 Microwave absorption properties

Microwave absorption properties of the Fe_3O_4@SnO_2 microspheres were investigated by the coaxial line method

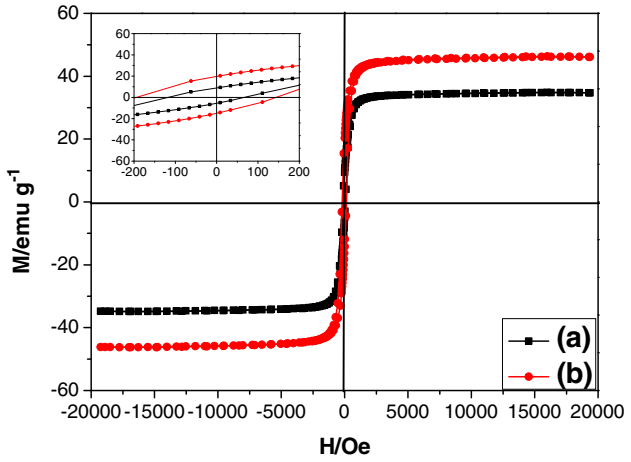

Fig. 6 Magnetic hysteresis loops of the Fe_3O_4@SnO_2 core–shell microspheres: (*a*) Fe_3O_4@SnO_2-1, (*b*) Fe_3O_4@SnO_2-2

Table 1 Magnetic parameters of the Fe_3O_4@SnO_2 nanospheres with different Fe_3O_4 core sizes

Samples (nm)	Parameters		
	Ms (emu/g)	*Hc* (Oe)	*Mr* (emu/g)
130	34.865	91.951	7.228
240	46.284	95.108	11.245

using an Agilent E8363A vector network analyzer at the range of 2–18 GHz under room temperature. The reflection loss (R_L) values of the samples can be calculated by Matlab using the complex permittivity ($\varepsilon_r = \varepsilon' - j\varepsilon''$) and permeability ($\mu_r = \mu' - j\mu''$) at a given frequency and absorber thickness according to the transmit-line theory [23], which is summarized as the following equations:

$$Z_{in} = (\mu_r/\varepsilon_r)^{1/2}\tanh\left[j(2\pi fd/c)(\mu_r\varepsilon_r)^{1/2}\right] \quad (1)$$

$$R_L(dB) = 20\log\left|\frac{Z_{in}-1}{Z_{in}+1}\right| \quad (2)$$

where Z_{in} is the input impedance of the absorber, μ_r and ε_r are respectively the relative complex permeability and permittivity of the absorber sample, f is the frequency of microwaves, d is the thickness of the absorber and c is the velocity of electromagnetic wave in free space.

Figure 7 shows the calculated frequency dependence reflection loss of the prepared samples with the sample thickness ranging from 1.5 to 5.5 mm. It can be found that the microwave absorption peaks of the samples move to low frequencies with increasing thickness, which can be explained by the formula of $f_m = c/(2\pi\mu''d)$ [24, 25]. When the matching thickness is 5.5 mm, Fe_3O_4@SnO_2-1 exhibit the maximum R_L of −37 dB at 5.3 GHz, which means more than 99 % of the incident EM-wave is absorbed.

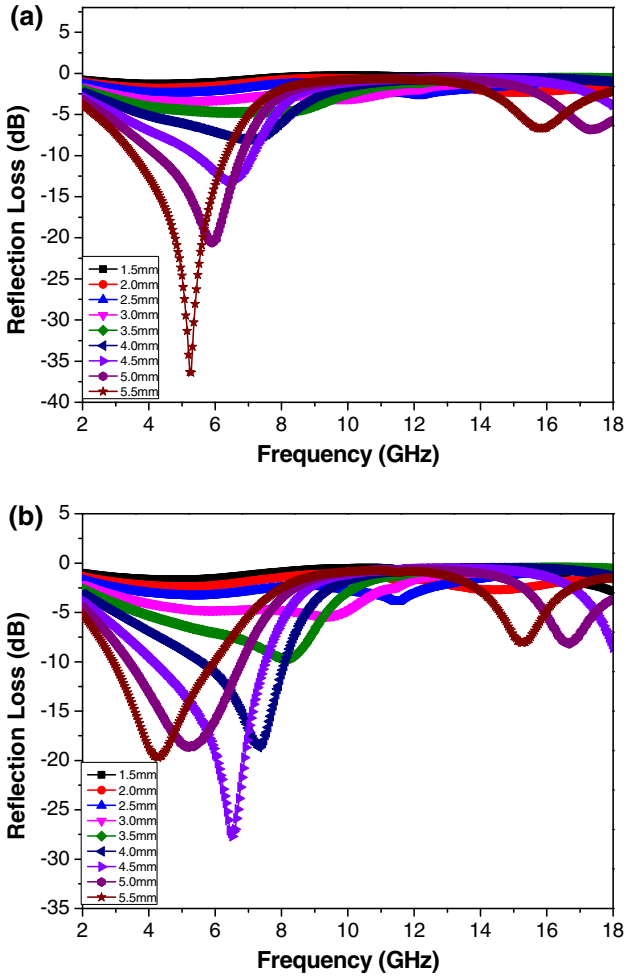

Fig. 7 Microwave reflection loss curves of the Fe_3O_4@SnO_2 core–shell microspheres: **a** Fe_3O_4@SnO_2-1, **b** Fe_3O_4@SnO_2-2

Moreover, the bandwidth of $R_L < -10$ dB (90 % absorption) can reach 4.3 GHz (ranging from 3.3 to 7.6 GHz) with a thickness in the range of 1.5–5.5 mm (Fig. 7a). The maximum R_L of Fe_3O_4@SnO_2-2 reached −28 dB (>99 % absorption) at 6.5 GHz for sample thickness of 4.5 mm. A bandwidth of $R_L < -10$ dB can reach 5.2 GHz (ranging from 3.0 to 8.2 GHz) with a thickness in the range of 1.5–5.5 mm (Fig. 7b). As previously stated, we conclude that the Fe_3O_4@SnO_2 microspheres exhibit extraordinary microwave absorption properties at the low frequency range.

It is well known that the good microwave absorption materials should meet the following requirements: firstly, the characteristic impedance of materials should be equal to the impedance of free air so that the microwave could enter the materials with the maximum intensity; secondly, the incident microwave should be absorbed with maximum intensity when they enter the absorbing materials [26, 27]. Figure 8 shows the frequency dependence of the complex

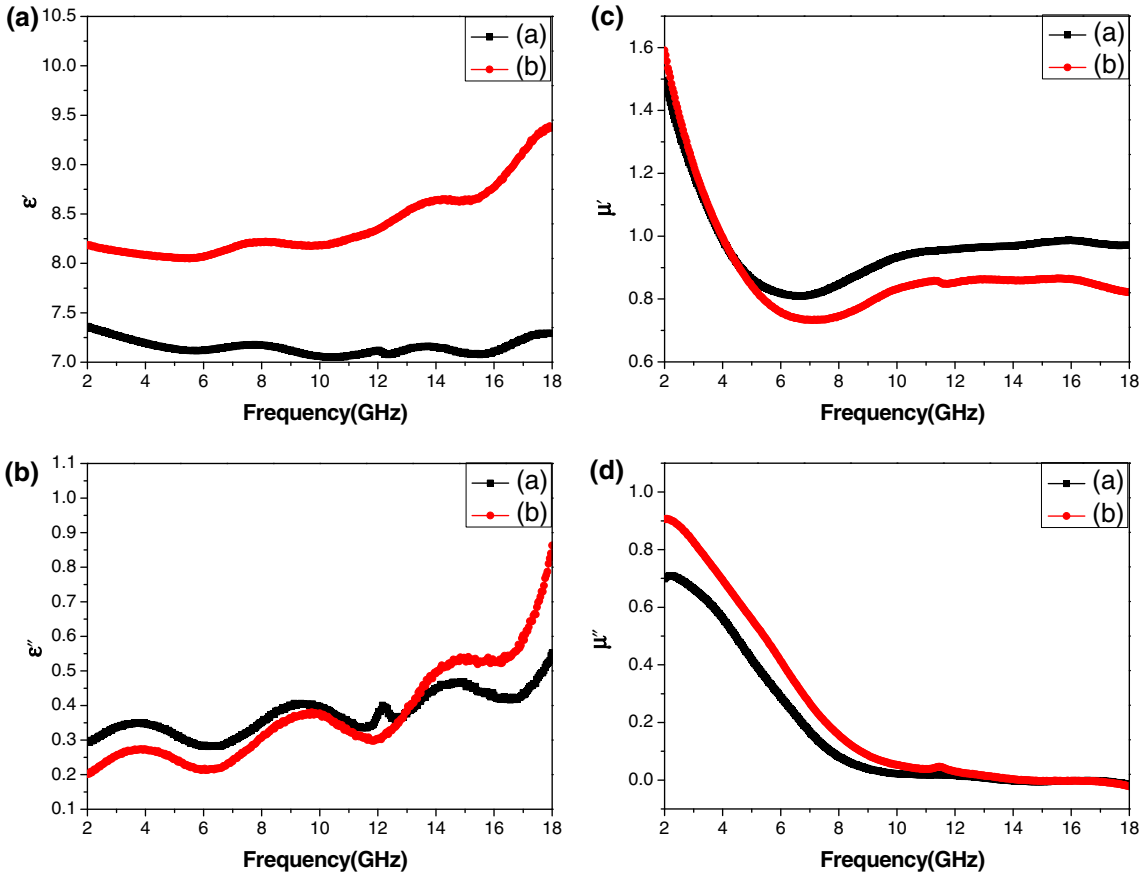

Fig. 8 Frequency dependence of the real part of complex permittivity ε′ (**a**), the imaginary part of complex permittivity ε″ (**b**), the real part of complex permeability μ′ (**c**) and the imaginary part of complex permeability μ″ (**d**) of the Fe_3O_4@SnO_2 core–shell microspheres: (*a*) Fe_3O_4@SnO_2-1, (*b*) Fe_3O_4@SnO_2-2

permittivity ε ($\varepsilon = \varepsilon' - j\varepsilon''$) and permeability μ ($\mu = \mu' - j\mu''$) of the samples. As we known, the real parts of complex permittivity (ε') and permeability (μ') symbolize the storage of electric and magnetic energy, respectively. While the imaginary parts of complex permittivity (ε'') and permeability (μ'') symbolize the loss of electric and magnetic energy, respectively [22]. It can be seen that the values of ε' for the Fe_3O_4@SnO_2-1 and Fe_3O_4@SnO_2-2 microspheres are in the range of 7.0–7.4 and 8.0–9.4, respectively, over the 2–18 GHz frequency range. The ε' values of Fe_3O_4@SnO_2-2 are relatively higher than Fe_3O_4@SnO_2-1, which may result from the different core sizes. The values of ε'' are in the range of 0.2–0.9. Meanwhile, it can be noticed that the curves of ε'' exhibit increase trend with the increasing frequency. Both the values of ε' and ε'' have some variation over the 2–18 GHz frequency range. In general, the fluctuating loss was attributed to the interfacial polarization and the lags of the polarization [28, 29]. Therefore, the interfaces between Fe_3O_4 microspheres and SnO_2 nanoparticles and polarization in Fe_3O_4 microspheres might be the reason for the small resonance peaks. As we known, the polarization in ferrites has largely been attributed to the presence of Fe^{2+} ions which give rise to heterogeneous spinel structure. Since Fe^{2+} ions are easily polarization, the larger the number of Fe^{2+} ions the higher would be the dielectric constant [30]. The values of μ' for the Fe_3O_4@SnO_2-1 and Fe_3O_4@SnO_2-2 microspheres are in the range of 0.8–1.5 and 0.7–1.6, respectively, over the 2–18 GHz frequency range. The μ' decreased sharply in the 2–7 GHz frequency range and then increased slightly in the 7–16 GHz frequency range, and reached their minimum values at 7 GHz. The μ'' exhibit the maximum value at 2.0 GHz and then decreased sharply in the 2–8 GHz frequency range. Because of the frequency range less 2.0 GHz is the natural resonance frequency of spinel ferrite, the maximum value of μ' and μ'' appearing at 2 GHz implies that the natural resonance occurred in the present Fe_3O_4@SnO_2 microspheres [31]. It is believed that natural resonance results in strong magnetic loss, implying enhanced microwave absorption by the Fe_3O_4@SnO_2 microspheres as electromagnetic energy is converted into heat energy [32]. Interestingly, it is

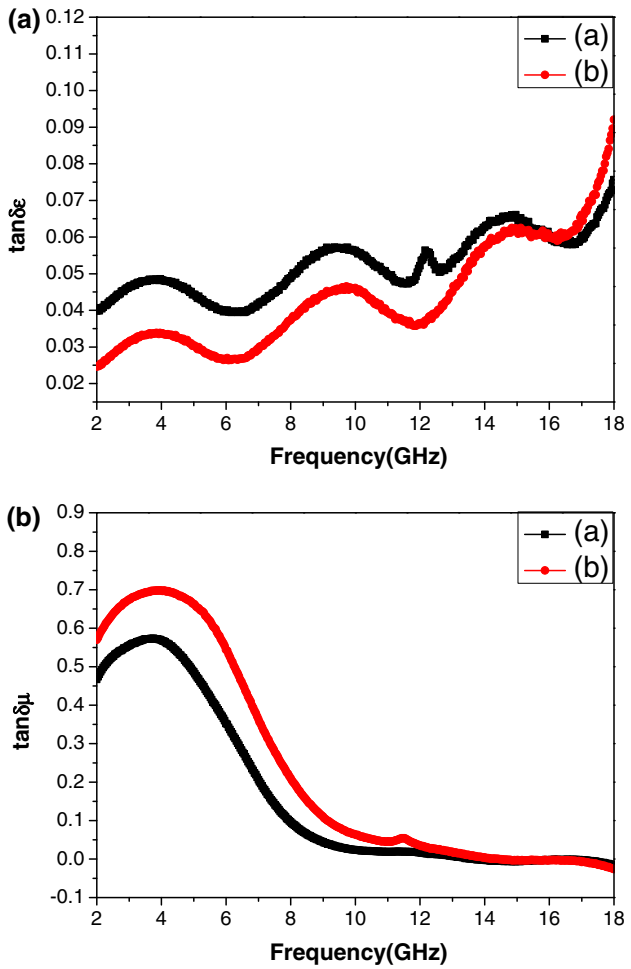

Fig. 9 Frequency dependence of the dielectric loss tangent (**a**) and the magnetic loss tangent (**b**) of the Fe_3O_4@SnO_2 core–shell microspheres: (*a*) Fe_3O_4@SnO_2-1, (*b*) Fe_3O_4@SnO_2-2

observed that the imaginary permeability of the samples is negative between 13.0 and 18.0 GHz. Generally, for left-hand materials both permittivity and permeability are negative. Therefore, the phenomenon should not be attributed to left-hand properties of the materials. Similar phenomenon was also found in some studies for various composites [12, 22]. They explained the phenomenon as the magnetic energy being radiated out form the composites and the more detail mechanism needs further study. To further study the intrinsic reasons for microwave absorption of the Fe_3O_4@SnO_2 microspheres, we calculate the dielectric tangent loss ($tan\delta_e = \varepsilon'/\varepsilon''$) and magnetic tangent loss ($tan\delta_m = \mu'/\mu''$). Figure 9 shows the frequency dependence of the dielectric loss tangent and magnetic loss tangent of the samples. The curves of $tan\delta_e$ exhibit increase trend with the increasing frequency, while the values of $tan\delta_m$ increased first and then decreased. It is obvious that $tan\delta_m$ is larger than $tan\delta_e$ at the low frequency range (2–8 GHz) and shows the maximum value at about 4 GHz. This reveals that the magnetic loss played the main role in the microwave absorption at the low frequency range (2–8 GHz). On the contrary, the dielectric loss became dominant at the high frequency range (8–18 GHz), whereas the absorbing effect is not ideal. Thus it is evident that the microwave absorption properties of Fe_3O_4@SnO_2 microspheres were determined by the integrated result of dielectric loss and magnetic loss. Appropriate match between the complex permittivity and permeability causes the excellent microwave absorption properties. Further study is in progress to adjust the permeability and permittivity to expand absorbing bandwidth.

4 Conclusions

In summary, the Fe_3O_4@SnO_2 core–shell structured microspheres with different Fe_3O_4 core sizes were successfully synthesized by hydrothermal method. Characterization techniques show that the microspheres are monodispersed, rough surfaces and ferromagnetic behavior at room temperature. Furthermore, the complex permittivity and permeability of the samples were measured and the microwave absorption properties were calculated using the absorbing-wall theory. It is found that the microspheres exhibited extraordinary microwave absorption properties at the low frequency range, which may result from the dielectric loss ability of SnO_2, unique core–shell structure and efficient complementarities between the relative permittivity and permeability in materials. Such results indicate that the Fe_3O_4@SnO_2 microspheres may become attractive candidates for microwave absorption materials.

Acknowledgments This work was supported by the National Natural Science Foundation of China (50972060), the Fundamental Research Foundation of the Central Universities (30920130112003), the Weapon Research Support Fund (62201070804), the Fundamental Product Innovation Research Project, and the Priority Academic Program Development of Jiangsu Higher Education Institutions (PAPD). The financial support is gratefully appreciated.

References

1. C. Sun, W. Jiang, Y.J. Wang, D.P. Sun, J. Liu, P.Y. Li, F.S. Li, Phys. Status Solidi-R **8**, 141 (2014)
2. B. Zhao, G. Shao, B.B. Fan, B. Sun, K.K. Guan, R. Zhang, J. Mater. Sci.: Mater. Electron. **25**, 3614 (2014)
3. D.P. Sun, Q. Zou, G.Q. Qian, C. Sun, W. Jiang, F.S. Li, Acta Mater. **61**, 5829 (2013)
4. R. Zhao, K. Jia, J.J. Wei, J.X. Pu, X.B. Liu, Mater. Lett. **64**, 457 (2010)
5. H.T. Feng, R.F. Zhuo, J.T. Chen, D. Yan, J.J. Feng, H.J. Li, S. Cheng, Z.G. Wu, J. Wang, P.X. Yan, Nanoscale Res. Lett. **4**, 1452 (2009)
6. P.C. Lian, S.Z. Liang, X.F. Zhu, W.S. Yang, H.H. Wang, Electrochim. Acta **58**, 81 (2011)

7. X.G. Liu, D.Y. Geng, H. Meng, P.J. Shang, Z.D. Zhang, Appl. Phys. Lett. **92**, 173117 (2008)
8. Z. He, S.H. Qi, X.L. Zhong, H. Oiu, J. Wang, J. Mater. Sci.: Mater. Electron. **25**, 3455 (2014)
9. H.L. Ding, Y.X. Zhang, S. Wang, J.M. Xu, S.C. Xu, G.H. Li, Chem. Mater. **24**, 4572 (2012)
10. J.Q. Wan, H. Li, K.Z. Chen, Mater. Chem. Phys. **114**, 30 (2009)
11. J.W. Liu, J.J. Xu, R.C. Che, H.J. Chen, M.M. Liu, Z.W. Liu, Chem. Eur. J. **19**, 6746 (2013)
12. Y.J. Chen, P. Gao, R.X. Wang, C.L. Zhu, L.J. Wang, M.S. Cao, H.B. Jin, J. Phys. Chem. C **113**, 10063 (2009)
13. W.W. Wang, J.L. Yao, J. Phys. Chem. C **113**, 3070 (2009)
14. C. Karunakaran, S. SakthiRaadha, P. Gomathisankar, P. Vinayagamoorthy, Powder Technol. **246**, 635 (2013)
15. R.Z. Li, X. Ren, F. Zhang, C. Du, J.P. Liu, Chem. Commun. **48**, 5010 (2012)
16. G.B. Sun, B.X. Dong, M.H. Cao, B.Q. Wei, C.W. Hu, Chem. Mater. **23**, 1591 (2011)
17. D.P. Sun, Q. Zou, Y.P. Wang, Y.J. Wang, W. Jiang, F.S. Li, Nanoscale **6**, 6557 (2014)
18. Y. Chen, B.H. Song, L. Lu, J.M. Xue, Mater. Technol. **28**, 255 (2013)
19. R. Zhao, K. Jia, J.J. Wei, J.X. Pu, X.B. Liu, Mater. Lett. **64**, 458 (2010)
20. D.W. Qi, J. Lu, C.H. Deng, X.M. Zhang, J. Phys. Chem. C **113**, 15858 (2009)
21. M. Parthibavarman, K. Vallalperuman, S. Sathishkumar, M. Durairaj, K. Thavamani, J. Mater. Sci.: Mater. Electron. **25**, 734 (2014)
22. Y.B. Li, G. Chen, Q.H. Li, G.Z. Qiu, X.H. Liu, J. Alloys Compd. **509**, 4106 (2011)
23. P.A. Miles, W.B. Westphal, A. Von Hippel, Rev. Mod. Phys. **29**, 280 (1957)
24. X.F. Zhang, X.L. Dong, H. Huang, Y.Y. Liu, W.N. Wang, X.G. Zhu, B. Lv, J.P. Lei, Appl. Phys. Lett. **89**, 053115 (2006)
25. Z.F. He, Y. Fang, X.J. Wang, H. Pang, Synth. Met. **161**, 424 (2011)
26. G.P. Zheng, X.W. Yin, S.H. Liu, X.M. Liu, J.L. Deng, Q. Li, J. Am. Ceram. Soc. **33**, 2178 (2013)
27. T. Chen, J.H. Qiu, K.J. Zhu, Y.C. Che, Y. Zhang, J.M. Zhang, H. Li, F. Wang, Z.Z. Wang, J. Mater. Sci.: Mater. Electron. **25**, 3672 (2014)
28. X.L. Dong, X.F. Zhang, H. Huang, F. Zuo, Appl. Phys. Lett. **92**, 013127 (2008)
29. C.C. Lee, D.H. Chen, Appl. Phys. Lett. **90**, 193102 (2007)
30. S.B. Ni, X.L. Sun, X.H. Wang, G. Zhou, F. Yang, J.M. Wang, D.Y. He, Mater. Chem. Phys. **124**, 355 (2010)
31. Y.M. Wang, Z. Luo, R.Y. Hong, Mater. Lett. **65**, 3243 (2011)
32. Y.F. Zhu, L. Zhang, T. Natsuki, Y.Q. Fu, Q.Q. Ni, Synth. Met. **162**, 342 (2012)